Environmental Science and Pollution Research (2020) 27:13114–13130
https://doi.org/10.1007/s11356-020-07796-3

RESEARCH ARTICLE

Comparative adsorption capabilities of rubbish tissue paper–derived carbon-doped MgO and $CaCO_3$ for EBT and U(VI), studied by batch, spectroscopy and DFT calculations

Ayub Khan[1] · Dongli Wei[1] · Fazli Khuda[2] · Ran Ma[1] · Muhammad Ismail[1] · Yuejie Ai[1]

Received: 13 October 2019 / Accepted: 21 January 2020 / Published online: 3 February 2020
© Springer-Verlag GmbH Germany, part of Springer Nature 2020

Abstract

Water pollution due to organic dyes and radionuclides is a challenging issue to the modern world. Cheap and efficient adsorbents are needed for their removal from wastewaters. Carbon-doped magnesium oxide (C-MgO) and calcium carbonate (C-$CaCO_3$) were synthesized by the in situ hydrothermal treatment of $Mg(OH)_2$ and $Ca(OH)_2$ with carbon, and applied for the removal of eriochrome black T (EBT) at pH = 2.0 and uranium (U(VI)) at pH = 6.0. The Langmuir monolayer adsorption capacities of C-MgO (3.62×10^{-4} mol/g for EBT and 8.10×10^{-4} mol/g for U(VI)) were higher than those of C-$CaCO_3$ (2.53×10^{-4} mol/g for EBT and 5.92×10^{-4} mol/g for U(VI)). The high adsorption capacity of C-MgO was also evidenced with DFT calculations which showed that the sorption energies (ΔE) of C-MgO for EBT (20.62 kcal/mol) and U(VI) (63.41 kcal/mol) were higher than those of C-$CaCO_3$ for EBT (10.21 kcal/mol) and U(VI) (34.29 kcal/mol). In all cases, the electrostatic interactions were involved in the adsorption process. The sorption kinetic data followed pseudo-second-order kinetics. The results demonstrate that both C-MgO and C-$CaCO_3$ are reusable and can be effectively applied for the elimination of EBT and U(VI) from wastewater.

Keywords Rubbish tissue papers · C-MgO · C-$CaCO_3$ · Adsorption · DFT · Reusability

Introduction

Water contamination due to organic dyes and radionuclides is a challenging issue for the modern world. Different industries such as pharmaceutical, food, paper and leather industries use large quantities of dyes. Particularly, textile industries have largely increased dyes in their effluents in terms of both types and volume (Robinson et al. 2001). According to an estimation, about 10,000 tonnes of dyes of different varieties are produced every year in the world (Forgacs et al. 2004). About 15% of these dyes flow into the industrial effluents, which cause turbidity and reduce the penetration of sun rays deep into the water (Houas et al. 2001). This affects aquatic plants by decreasing the rate of photosynthesis in them. Consequently, the deoxygenation of water disturbs life activities in fish and other aquatic animals. Furthermore, organic dyes can also enter the food chain and distress human health as well as local flora and fauna (Khurana et al. 2018).

Apart from dyes, radionuclides such as U(VI) is a serious cause of environmental pollution. Nuclear technology plays an important role in agriculture, power and defence system of a country. However, nuclear power plants, nuclear weapon test sites, uranium ore processing and weathering of rocks are important sources of uranium in the environment (Child and Hotchkis 2013). ^{235}U and ^{238}U are the natural radioactive forms of uranium with a half-life of 7.0×10^8 and 4.4×10^9 years, respectively. Therefore, they exist for a long period of time in the environment and eventually accumulate in the plants and animals and cause toxic health problems in them. In

Responsible editor: Tito Roberto Cadaval Jr

Electronic supplementary material The online version of this article (https://doi.org/10.1007/s11356-020-07796-3) contains supplementary material, which is available to authorized users.

✉ Ayub Khan
ayubkhanjf@hotmail.com

✉ Yuejie Ai
aiyuejie@ncepu.edu.cn

[1] College of Environmental Science and Engineering, North China Electric Power University, Beijing 102206, People's Republic of China

[2] Department of Pharmacy, University of Peshawar, Peshawar, Khyber Pakhtunkhwa 25120, Pakistan

animals and humans, they are absorbed in the gastrointestinal tract via drinking water or food and cause kidney failure in them (Bayramoglu et al. 2015; Konietzka 2015). They enter the plants via the root system and accumulate in their different parts (Dushenkov et al. 1997). Health problems due to organic dyes and uranium emphasize their removal from contaminated water and have become the focus of worldwide research topics.

Among the many methods used for the removal of unwanted species from wastewater, the adsorption technique is easy, cost-effective, simple to operate and eco-friendly (Ayub et al. 2017; Khan et al. 2018). A variety of adsorbents such as activated carbons (de Luna et al. 2013) and double-layer hydroxide composites (Blaisi et al. 2018) have been applied for the removal of EBT from aqueous solutions. Similarly, coal fly ashes (Chen et al. 2017) and layered titanate nanowires (Yin et al. 2017) have been utilized for the removal of U(VI) from water solutions. However, these adsorbents had no prominent bonding sites for EBT and U(VI) ions. On the other hand, EBT and U(VI) could form strong complexes with magnesium and calcium ions. Moreover, the carbon-loaded adsorbents have remarkable adsorption capabilities for U(VI) (Liao et al. 2019). Therefore, we proposed to use rubbish tissue paper–derived carbon-doped MgO and $CaCO_3$ for the elimination of EBT and U(VI) from aqueous environment.

The morphologies and physical properties of MgO and $CaCO_3$ are dependent on their way of preparation. Calcination of $Mg(OH)_2$ in air at 450°C results in a blur mass of MgO powders (Moussavi and Mahmoudi 2009). The sol-gel combustion of $Mg(NO_3)_2$ with urea, citric acid and oxalic acid at 350°C results in irregular cubes of MgO (Nassar et al. 2017). Similarly, the morphology of $CaCO_3$ depends on the reaction temperature (Seo et al. 2005). $CaCO_3$ obtained by the simultaneous mixing of $CaCl_2$ with NH_4HCO_3 (1:1 ratio) at 30°C had mushroom-like lamellar structures with a diameter of 20–35 μm (Chen and Xiang 2009). The diameter of the particles decreased to 10–20 μm when the temperature was increased to 50°C. The morphology changed to rod shape at 60°C. Similarly, rod-shaped crystals with a constant diameter of 1.0–5.0 μm and a length of 15–40 μm were formed at 80°C. Recently, we synthesized them by using a different approach. Firstly, we achieved amorphous carbon by the wet oxidation of rubbish tissue papers. Then it was used as reducing as well as doping agent in the in situ hydrothermal treatment of $Mg(OH)_2$ and $Ca(OH)_2$ to obtain C-MgO and C-$CaCO_3$. The C-MgO and C-$CaCO_3$ achieved in this way had unique morphologies. Here carbon played the following significant roles: (I) At high temperature and pressure, carbon reacts with water and in a series of reactions might produce certain gases such as water gas and carbon dioxide gas, which could react with $Mg(OH)_2$ and $Ca(OH)_2$ to form MgO and $CaCO_3$; (II) Doping with carbon reduces the sticky and gelatinous nature of MgO and $CaCO_3$ in aqueous solutions and gives them unique morphologies; (III) Doping with carbon changes the pH_{pzc} values of $CaCO_3$ and MgO and consequently changes their adsorption properties. Both naked $CaCO_3$ and MgO are suitable for the adsorption of anions only (Hu et al. 2010; Smiciklas et al. 2008), whereas C-$CaCO_3$ and C-MgO are found to be suitable for the adsorption of both anions and cations.

Although numerous studies on U(VI) and EBT sorption are reported in the literature, the interaction mechanisms of EBT and U(VI) with C-MgO or C-$CaCO_3$ have not been investigated theoretically. This study performs density functional theory (DFT) calculations to elucidate molecular-level interactions between C-MgO/C-$CaCO_3$ and EBT/U(VI). Such interactions are difficult to ascertain experimentally. However, computational chemistry provides a great help in the study of molecular-level interactions and provides an easy, quick and cheap way to explain the interaction mechanism between pollutants and adsorbents.

The purpose of this study is to introduce a new and economic way for the synthesis of C-MgO and C-$CaCO_3$ and their comparative adsorption capacities for the removal of EBT and U(VI) from wastewater. It was also intended to reuse the rubbish tissue papers for more valuable purposes in the synthesis and doping of MgO and $CaCO_3$. The adsorption capabilities of C-MgO and C-$CaCO_3$ for EBT and U(VI) have been optimized under different experimental conditions. The structures, energies, electronic properties and adsorption behaviour of EBT and U(VI) onto C-MgO and C-$CaCO_3$ are also elucidated by DFT simulations.

Materials and methods

Synthesis of carbon

The reagents utilized in the batch sorption study of EBT/U(VI) onto C-MgO/C-$CaCO_3$ were obtained from Sinopharm Chemical Regent Co., Ltd. (Beijing, China). Carbon was synthesized by the wet oxidation of rubbish tissue papers. In a typical reaction, 5.60 mL of conc. H_2SO_4 was slowly added to 5.0 g of the used tissue papers in a 200-mL beaker. The ingredients were continuously mixed with a wooden stick, and finally, the black powder was washed to the pH close to Milli-Q water. After drying at 110°C for 5.0 h, the product was grinded to a fine powder and stored in a plastic bag for further use.

Synthesis of C-MgO and C-$CaCO_3$

For this purpose, $MgCl_2.6H_2O$ (1.051 g, 5.17 mmol) and NaOH (0.414 g, 10.34 mmol) were separately added to 30 mL Milli-Q water. Then the $MgCl_2.6H_2O$ solution was added dropwise to NaOH solution under vigorous stirring.

After 30 min stirring at 40°C, the reaction mixture along with 0.5 g carbon was transferred to a Teflon-lined stainless-steel autoclave. The reaction mixture was subjected to 140°C for 6.0 h. The obtained C-MgO was washed three times with Milli-Q water and dried up at 110°C for 5.0 h. The same process, using $CaCl_2$ instead of $MgCl_2$, was repeated for the synthesis of C-$CaCO_3$. All the possible reactions involved in the conversion of $Mg(OH)_2$ and $Ca(OH)_2$ to C-MgO and C-$CaCO_3$ are presented in SI.

Characterization

The morphologies of the synthesized materials were characterized by scanning electron microscopy (S-2500, Japan) and transmission electron microscopy (TEM, Hitachi-7650). The BET surface area was measured by QUADRASORBSI, Quantachrome USA. The powder X-ray diffraction (XRD) pattern was performed with Rigaku-D/max2200 diffractometer in the 2θ range of 5–70° and a scanning rate of 0.05°/s. Fourier transform infrared (FT-IR) spectra were obtained by Nicolet Magana-IR 750 spectrometer. The thermogravimetric analysis (TGA) was performed with a Shimadzu TGA Q5000 thermal analyser in the range of 50–900°C and a heating rate of 10°C min^{-1}. The ZETASIZER 3000 HSA system was used for measuring the zeta potential values of the adsorbents. The XPS analysis was performed by Thermo Escalab 250 electron spectrometer operating at 150 W Al Kα radiation.

Batch sorption experiments

Batch sorption experiments for EBT and U(VI) were performed at different experimental conditions. Suitable amounts of EBT (2.17×10^{-5} to 5.85×10^{-4} mol/L) and U(VI) (2.54×10^{-5} to 2.79×10^{-4} mol/L) along with adsorbent (0.05 to 0.20 g/L) were transferred to a series of 10-mL polyethylene test tubes and diluted to the required concentrations. The adsorption was optimized by performing pH experiments in the range of 2.0–10.0. Small volumes of 0.1 mol/L HCl or NaOH were used to acquire the desired pH. The effect of adsorbent amount was accomplished in the range of 0.05–0.80 g/L. The kinetic experiments were conducted in the time range of 10 min to 13.0 h. The adsorption equilibria were achieved at 25, 40 and 55°C. The samples were gently shaken at 150 rpm in a thermostatic shaker in the dark to avoid photo-degradation of the pollutant species. After the equilibration time, the samples were filtered through Nylon-66 syringe filters (0.22 μm) to separate the adsorbent from the suspension. The concentration of U(VI) in the supernatant was determined with arsenazo-III spectrophotometric technique at 650 nm while that of EBT was recorded at 520 nm. The adsorption percentage was determined as adsorption (%) = $(C_o - C_e)/C_o \times 100$ while the equilibrium concentration was calculated as, $q_e = (C_o - C_e) \times V/m$, where C_o and C_e (mol/L), q_e (mol/g), V (L) and m (g) are the initial concentration, equilibrium concentration, adsorption amount at equilibrium, volume of the suspension and weight of the adsorbent, respectively.

Results and discussion

Characterization

The microstructures and surface characteristics of carbon, C-MgO and C-$CaCO_3$ were accomplished by SEM and TEM images. The SEM image (Fig. 1a) exposes amorphous morphology of granular carbon. The C-MgO had rod-shaped morphology (Fig. 1b), whereas C-$CaCO_3$ appeared as plate-like structures with well-defined edges (Fig. 1c). The TEM image of carbon (Fig. 1e) discloses the homogenously distributed granules. The rod-shaped C-MgO nanoparticles with lattice fringes of 1.70 Å were 63.31 nm long (Fig. S1a) and 7.71 nm wide (Fig. S1b) and were covered with carbon particles (Fig. 1f). The interplanar spacing of C-$CaCO_3$ (calcite) nanoplatelets was 2.77 Å (Fig. 1g) with an average diameter and a particle area of 53.23 nm and 1.89×10^{-6} m^2 (Fig. S1c and d), respectively. Moreover, the high-resolution transmission electron microscopy (HRTEM) images of the boxed area in Fig. 1 f and g confirmed the single-crystalline nature of C-MgO and C-$CaCO_3$ materials. The energy dispersive X-ray microanalysis (EDXMA, Fig. 1d, h) demonstrates the presence of carbon, magnesium and oxygen in C-MgO and carbon, calcium and oxygen in C-$CaCO_3$. Calculated from the EDXMA analysis, the concentrations of the surface carbon in C-MgO and C-$CaCO_3$ were 10.86 and 31.38 at%, respectively. The powder XRD patterns of the synthesized materials are shown in Fig. 2a. In the XRD pattern of carbon, the broad peak at $2\theta = 21.67^o$ indicates its amorphous nature (Rajan et al. 2014). The face-centred cubic-structured MgO nanorods with lattice parameter, $a = 4.21$ Å, had distinctive planes (111), (200), (220), (311) and (222) at $2\theta = 37.12°$, 43.04°, 62.26°, 74.68° and 79.08°, respectively (JCPDS PDF No. 00-001-1235) (Devi et al. 2012). The crystallite size of C-MgO calculated from the most intense peak (200) was 4.87 nm, whereas it was 5.0 nm for monocrystalline MgO achieved by sol-gel method (Goryczka et al. 2010). The major reflections for calcite, (104) and (110) appeared at $2\theta = 29.28°$ and 36.04°, respectively (JCPDS PDF No. 01-086-2340) (Peng et al. 2013). The lattice parameter (a) of C-$CaCO_3$ (calcite) was 9.76 Å with crystallite size of 18.38 nm. The sharp peaks in C-MgO and C-$CaCO_3$ XRD patterns indicated their ultra-fine nature. Furthermore, the XRD pattern evidenced that doping with carbon had no effect on the crystal structures and brought no structural deformations to MgO and $CaCO_3$.

In the FT-IR analysis of all the materials (Fig. 2b), the strong peak at 3434 cm^{-1} was due to the physically attached

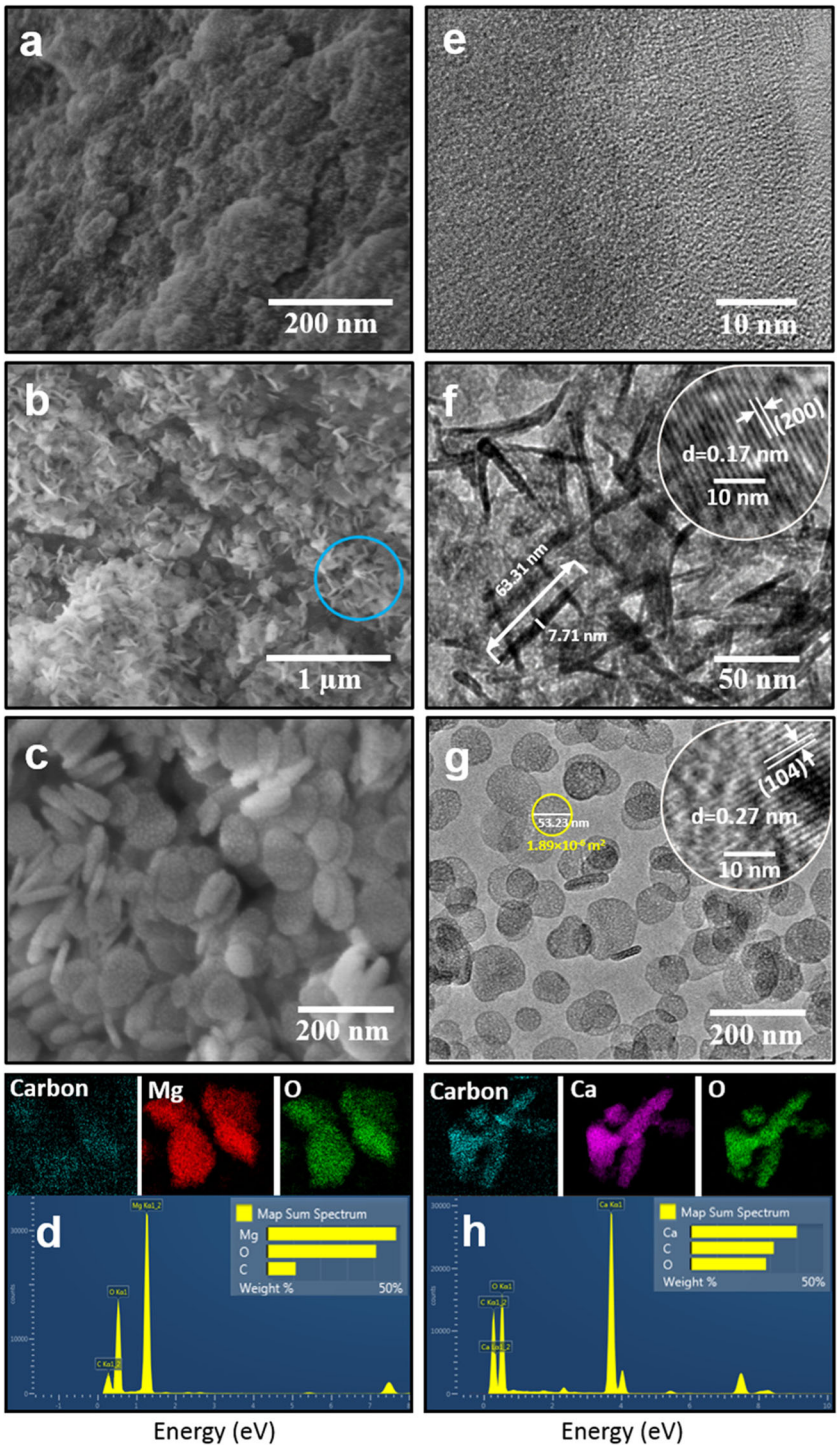

Fig. 1 SEM images of **a** carbon, **b** C-MgO and **c** C-$CaCO_3$. **d** Elemental mapping and EDX spectrum of C-MgO. TEM images of **e** carbon, **f** C-MgO and **g** C-$CaCO_3$. **h** Elemental mapping and EDX spectrum of C-$CaCO_3$

water molecules. In the FT-IR spectrum of C-MgO, a small peak at 1155 cm^{-1} corresponded to H^- ions bonded to Mg^{2+} at different coordination cites while the characteristic Mg-O stretching vibrations appeared at 430 cm^{-1} (Mageshwari et al. 2013). In the case of $CaCO_3$, a strong peak at 1404 cm^{-1} along with a shoulder peak (1510 cm^{-1}) was due to CO_3^{2-} ions (Wang et al. 2017). The other FT-IR characteristic peaks for $CaCO_3$ were found at 3441, 1461, 1037, 871 and 770 cm^{-1}, which were in good agreement with the reported result (Saraya and Rokbaa 2016).

The Brunauer-Emmett-Teller (BET) surface areas of pure carbon, C-MgO and C-$CaCO_3$ were found to be 24, 54 and 29

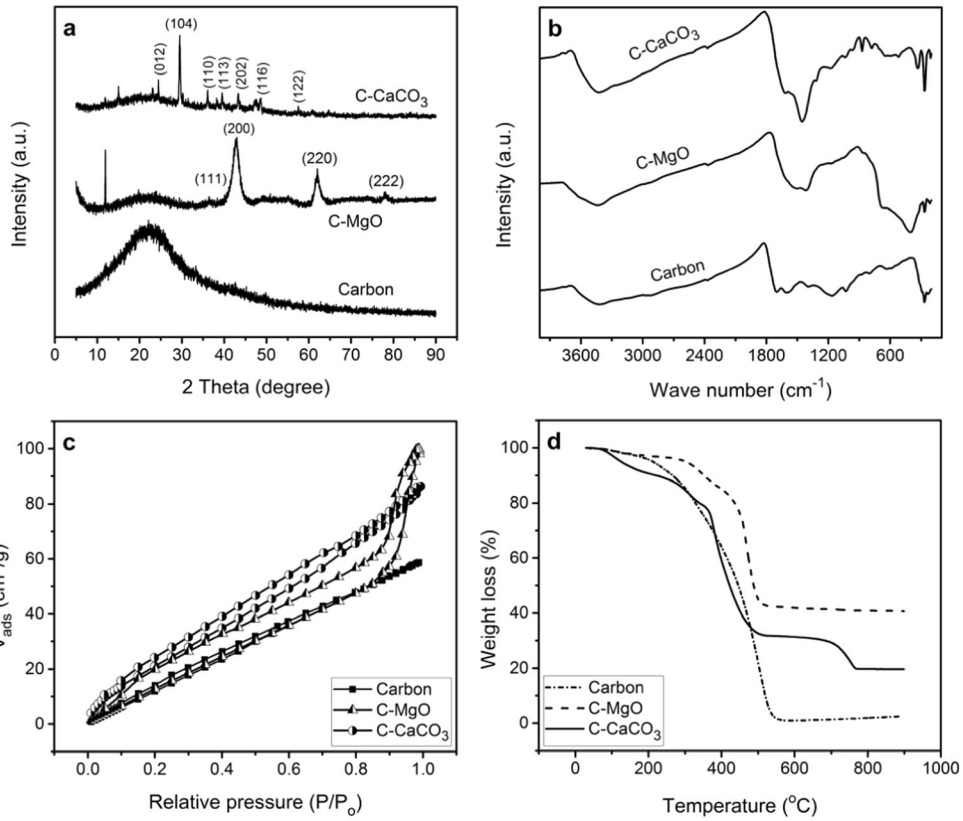

Fig. 2 **a** XRD patterns, **b** FT-IR spectra, **c** N_2 adsorption-desorption isotherms and **d** TGA curves of the synthesized materials

m^2/g (Fig. 2c) with the average pore diameters (Barrett-Joyner-Halenda (BJH)) of 3.7, 5.1 and 18.6 nm and total pore volumes of 0.091, 0.134 and 0.727 cm^3/g, respectively (Fig. S2). Larger pore diameters represented the mesoporous nature of the materials and were useful for the strong uptake of U(VI) and EBT. The pore diameters of both C-MgO and C-$CaCO_3$ were very large compared with the molecular diameter of EBT (1.55 nm) (Loera-Serna et al. 2017) and the ionic radius of U(VI) (0.086 nm) (Ohmichi et al. 1981). Therefore, it could be easy for EBT and U(VI) to diffuse inside the adsorbent materials.

The TGA curve (Fig. 2d) shows that the oxidation of pure carbon completed at 550°C and entirely converted to CO_2 gas (Oliveira et al. 2002). The physically adsorbed water molecules were detached (5% weight loss) from C-MgO at 200°C followed by the evolution of CO_2 gas (55% weight loss) at 500°C, leaving behind a constant mass of MgO (40% weight) as solid residue. Till 500°C, the TGA thermograph of C-$CaCO_3$ was similar to that of C-MgO. The moisture content was lost in the first jump. Carbon was removed in the second step to form CO_2 gas (60% weight loss). In the third step, at 770°C, the remaining $CaCO_3$ started to decompose into CaO (20% constant mass left behind) and CO_2 gas (10% weight loss). The possible reactions that carbon, C-MgO and C-$CaCO_3$ might have undergone during thermogravimetric analysis, are presented in SI.

pH_{pzc} is an important characteristic property of an adsorbent and determines its adsorption mode towards a pollutant. The pH_{pzc} of pure carbon is neutral (7.0) or slightly basic (7.9) (Hao et al. 2004; Kodama and Sekiguchi 2006). The pH_{pzc} value of naked $CaCO_3$ lies in the range of 8.0–9.5 (Smiciklas et al. 2008) while that of naked MgO is 12.4 and is favourable for the adsorption of anions only (Hu et al. 2010). Interestingly, the pH_{pzc} of C-$CaCO_3$ and C-MgO are 2.50 and 3.34, respectively, and allow the adsorption of both anions (such as EBT) and cations (such as UO_2^{2+}).

XPS analysis was performed to characterize the surface states of the as-prepared materials. The survey spectra of C-MgO and C-$CaCO_3$ (Fig. 3a) show distinct peaks at 49.86 eV (Mg 2p) and 347.42 eV (Ca 2p). The Mg 2p peak in C-MgO spectrum at 49.4 eV was assigned to magnesium-bonded hydroxyl groups (Mg-OH), while the peak at 50.5 eV was assigned to magnesium-bonded oxygen atoms (Mg-O, Fig. 3b) (Li et al. 2014). The C 1s peak of each material was deconvoluted into several Gaussian peaks. The carbon peaks were found in binding energy range from 281.0–292.0 eV (Fig. 3c). In the C 1s spectrum of MgO (111) surface, four different peaks at 284.6, 286.2, 288.0 and 290.3 eV, were assigned to C-C, C-O, C=O and O-C=O, respectively (Zou et al. 2017). The Mg 1s peak at 1303 eV was supplemented by Auger peaks between 300 and 390 eV (encircled area in Fig. 3a which is enlarged in

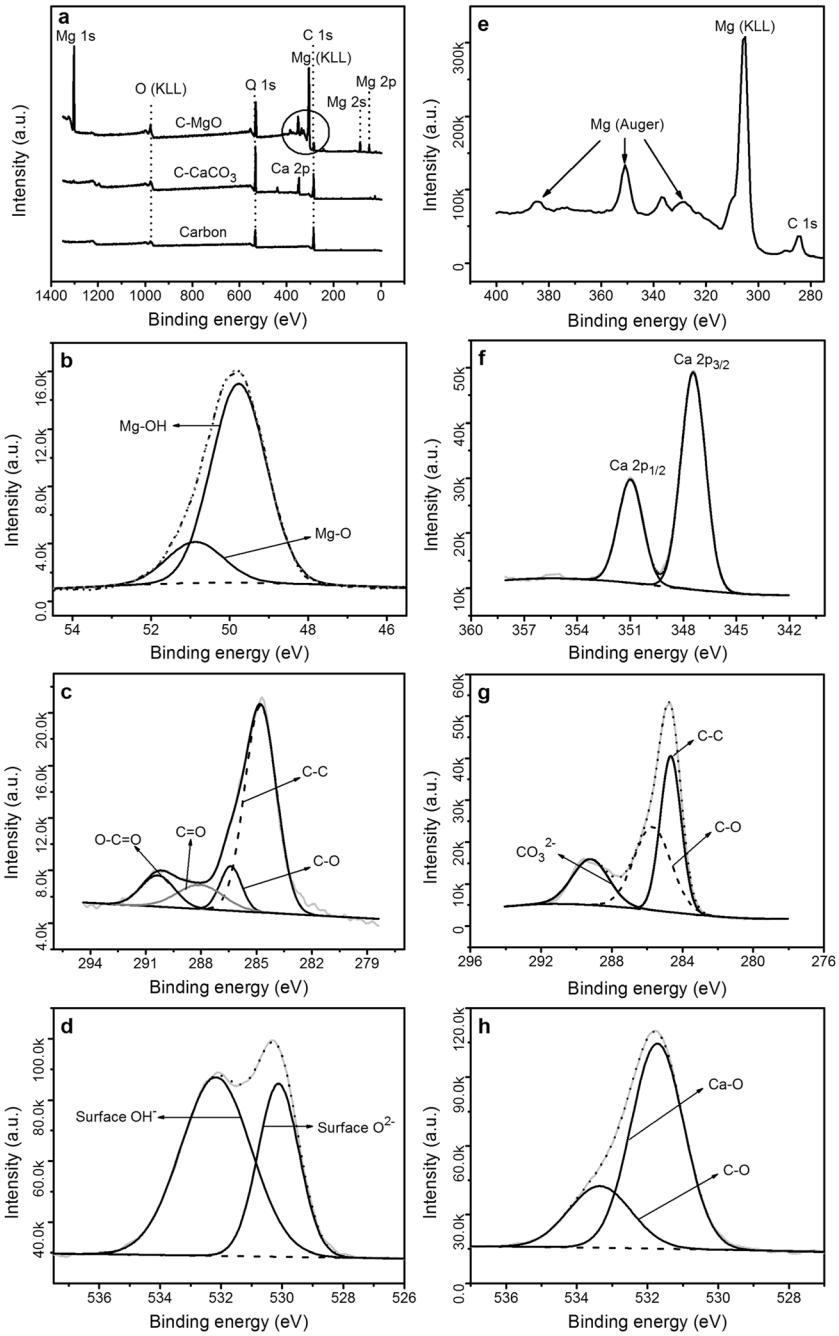

Fig. 3 **a** XPS survey scan spectra of adsorbent materials, **b** XPS spectra of Mg 2p, **c** C 1s, **d** O 1s and **e** Mg (KLL) and Auger peaks of C-MgO. XPS spectra of **f** Ca 2p, **g** C 1s and **h** O 1s of C-$CaCO_3$. **e** is the enlarged photo of the encircled area in **a**

Fig. 3e). The Auger peaks have large chemical shifts and are useful for chemical state analysis. The O 1s XPS spectrum of C-MgO (Fig. 3d) was deconvoluted into two components at 530.1 eV (surface oxide O^{2-}) and 532.1 eV (surface OH^{-}) (Cui et al. 2018; Yao et al. 2000). The peak at higher binding energy was due to chemisorbed water. As shown in the survey spectrum, the Ca 2p and Mg (KLL) peaks can be easily misunderstood, because Ca 2p appears in the range same to that of Mg Auger peaks. However, the characteristic spin-orbit splitting of the suspected Ca 2p peak (Ca $2p_{3/2}$ and Ca $2p_{1/2}$ components) splits by 3.4 eV with an intensity ratio of 2:1. The presence of Ca $2p_{3/2}$ at 347.42 eV and Ca $2p_{1/2}$ at 350.03 eV (Chen et al. 2018), in the high-resolution XPS spectrum of Ca 2p (Fig. 3f), confirmed the existence of $CaCO_3$ in the sample. C 1s spectrum of C-$CaCO_3$ (Fig. 3g) was deconvoluted into three Gaussian peaks at 284.6 eV (C-C), 285.6 eV (C-O) and 289.2 eV (CO_3^{2-}), with full width at half maximum (FWHM) values of 1.39, 2.45 and 2.43, respectively (Chu et al. 2013). The C-$CaCO_3$ O 1s XPS

spectrum (Fig. 3h) was deconvoluted into Ca-O (531.1 eV) and C-O (533.3 eV), with FWHM values of 1.76 and 2.07, respectively (Ni and Ratner 2008). This suggested that some Ca atoms on the surface of $CaCO_3$ existed in the oxide form. The percentage of different functional groups present in C-$CaCO_3$ and C-MgO, calculated from C 1s and O 1s peaks are shown in Fig. S3. The percent concentrations of C 1s deconvoluted peak areas of each functional group present in C-$CaCO_3$ were 40.70% (C-C), 20.94% (CO_3^{2-}) and 38.36% (C-O), and those of O 1s were 73.87% (Ca-O) and 26.13% (C-O) (Fig. S3a). The percent concentrations of C 1s deconvoluted peak areas assigned to each functional group in C-MgO were 67.71% (C-C), 9.93% (C-O), 11.55% (C=O), and 10.82% (O-C=O), and those of O 1s were 36.16% (O^{2-}) and 63.34% (OH^-) (Fig. S3b). High concentration of the surface bonded OH^- groups can prominently enhance the adsorption ability of C-MgO towards EBT and U(VI). The relative percent distribution of elements in both adsorbents is given in Table S1. The carbon content of C-MgO (10.36%) was less than that of C-$CaCO_3$ (31.38%). However, it was homogeneously distributed in C-MgO (Fig. 1d), while aggregated in C-$CaCO_3$ (Fig. 1h). The homogeneous distribution of carbon could be beneficial for the high surface area and adsorption capacity of C-MgO. The atomic ratios and binding energies of all elements in C-MgO and C-$CaCO_3$ are given in Table 1. Moreover, various metal oxides and their peak positions are tabulated in Table S2.

Effect of solid content

The effect of solid content was studied to achieve maximum adsorption of pollutants with minimum possible amount of adsorbent. Figure 4 a and b elucidate the effect of C-$CaCO_3$ and C-MgO dose on U(VI) sorption while their effect on EBT sorption is given in Fig. S4a and b. The experiments showed that the adsorption of EBT and U(VI) increased significantly with increasing the adsorbent amount from 0.05 to 0.20 g/L. Figure 4 a and b and Fig. S4a and b further illustrate that the partition ratio (K_d) increased proportionally with the increase in the amount of adsorbent till it reached 0.20 g/L and then decreased with further increase of the adsorbent amount. The maximum adsorption of both EBT and U(VI) was observed at 0.20 g/L of C-$CaCO_3$ and C-MgO.

Effect of solution pH

The pH of the solution has great impact on the adsorption properties and chemical state of an adsorbent. Similarly, it influences the distribution of organic and inorganic species in aqueous solutions. The effect of pH on the adsorption of EBT and U(VI), and the relative distribution of their species as a function of pH are shown in Fig. 4c and d. A rapid decrease in the adsorption of EBT onto C-$CaCO_3$ was observed when the pH was increased from 3.0 to 5.0 (Fig. 4c). This was because the surface of C-$CaCO_3$ was negatively charged at pH higher than its pH_{pzc} (2.50, Fig. 4e) which might lead to strong repulsions with EBT anions. Beyond pH = 3.0, the increase in negative charge on both adsorbents as well as EBT intensified the electrostatic repulsions between them. Consequently, the adsorption of EBT decreased continuously throughout the whole pH range. On the other hand, the adsorption of U(VI) followed a totally different route. Unlike EBT, the adsorption of U(VI) was low at low pH. However, it increased rapidly with increasing pH and reached to the peak value at pH = 6.0, followed by a gradual decrease. The relative distribution of U(VI) species (Fig. 4d) shows that at pH = 6.0, UO_2^{2+}, $(UO_2)_2(OH)_2^{2+}$ and $(UO_2)_3(OH)_5^+$ ions were dominant species in the solution. At low pH, the competition between H^+, Na^+ and UO_2^{2+} ions suppressed the sorption of UO_2^{2+} ions (Wang et al. 2016). The high adsorption efficiency at pH = 6.0 was due to the strong surface complexation and electrostatic interactions between the positively charged U(VI) species and the negatively charged C-$CaCO_3$ and C-MgO surfaces. At pH = 9.0–10.0, the electrostatic repulsion between U(VI) anions, i.e., $(UO_2)_3(OH)_7^-$, $UO_2(OH)_3^-$ and $(UO_2)(OH)_4^{2-}$ and the negatively charged adsorbents resulted in low adsorption (Ding et al. 2015). Figure 4f shows that the adsorption of U(VI) decreased only by 0.6% when the NaCl concentration increased from 0.001 to 0.03 mol/L. A small effect of ionic strength suggested the formation of inner-sphere surface complexes of U(VI) with both adsorbents (Hu et al. 2015). However, the gradual increase in the adsorption after 0.03 mol/L NaCl was due to the salting-out effect of NaCl (Chen et al. 2017).

Table 1 XPS surface elemental analysis of C-MgO and C-$CaCO_3$

Samples	Mg 2p		Ca 2p		C 1s		O 1s	
	at%	B.E (eV)	at%	B.E (eV)	at%	B.E (eV)	at%	B.E (eV)
C-MgO	23.18	49.86	–	–	17.59	284.79	34.23	531.77
C-$CaCO_3$	–	–	7.55	347.42	56.58	284.79	35.87	531.89

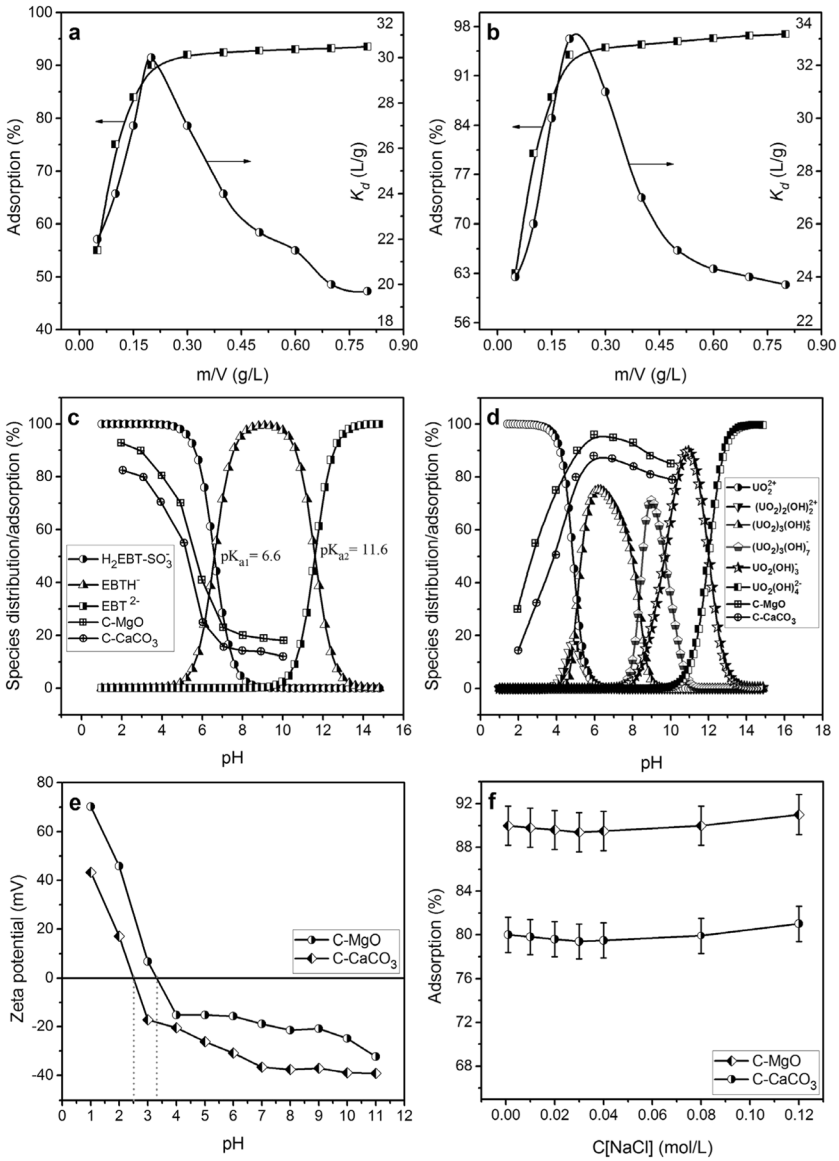

Fig. 4 Effect of the adsorbent dose on the adsorption and partition ratio of U(VI) onto **a** C-$CaCO_3$ and **b** C-MgO, at C_o[U(VI)] = 7.61×10^{-5} mol/L, pH = 6.0, C[NaCl] = 0.01 mol/L and T = 25 °C. Effect of pH on the speciation and adsorption of **c** EBT and **d** U(VI) at C_o[EBT] = 8.67×10^{-5} mol/L, C_o[U(VI)] = 7.61×10^{-5} mol/L, m/V = 0.20 g/L, T = 25°C (C[NaCl] = 0.01 mol/L for U(VI) only). **e** Determination of zeta potential as a function of pH in 0.01 mol/L NaCl solution. **f** Effect of ionic strength on U(VI) sorption at C_o[U(VI)] = 7.61×10^{-5} mol/L, m/V = 0.20 g/L and T = 25°C. The experimental conditions are not applicable to the speciation of EBT

Adsorption kinetics

Adsorption kinetics was helpful in explaining the basic steps such as mass transport and chemical reaction involved in the adsorption process. The pseudo-first-order model (PFO, Eq. (1)) (Vilela et al. 2018) and pseudo-second-order model (PSO, Eq. (2)) (Balasubramanian et al. 2019) were applied to investigate the kinetic data and are expressed as:

$$q_t = q_e\left(1-e^{-k_1 t}\right) \quad (1)$$

$$q_t = \frac{q_e^2 k_2 t}{1 + q_e k_2 t} \quad (2)$$

where q_e and q_t (mol/g) referred to the equilibrium and instantaneous adsorption of pollutants and k_1 (1/h) and k_2 (g/mol·h) are the PFO and PSO rate constants. Due to the availability of more binding sites on the adsorbent surface, the initial adsorption rate of EBT onto C-MgO and C-$CaCO_3$ was rapid and reached equilibrium in 2.5 and 3.3 h, respectively (Fig. 5a). Similarly, the equilibrium time for U(VI) onto C-MgO and C-$CaCO_3$ was 1.6 and 3.0 h, respectively (Fig. 5b). The respective values of q_e, k_1 and k_2 are listed in Table S3. It shows that the EBT and U(VI) sorption on C-MgO was faster than C-$CaCO_3$, i.e., $k_{C\text{-}MgO} > k_{C\text{-}CaCO3}$, which further confirmed that EBT and U(VI) sorption onto C-MgO was much efficient than C-

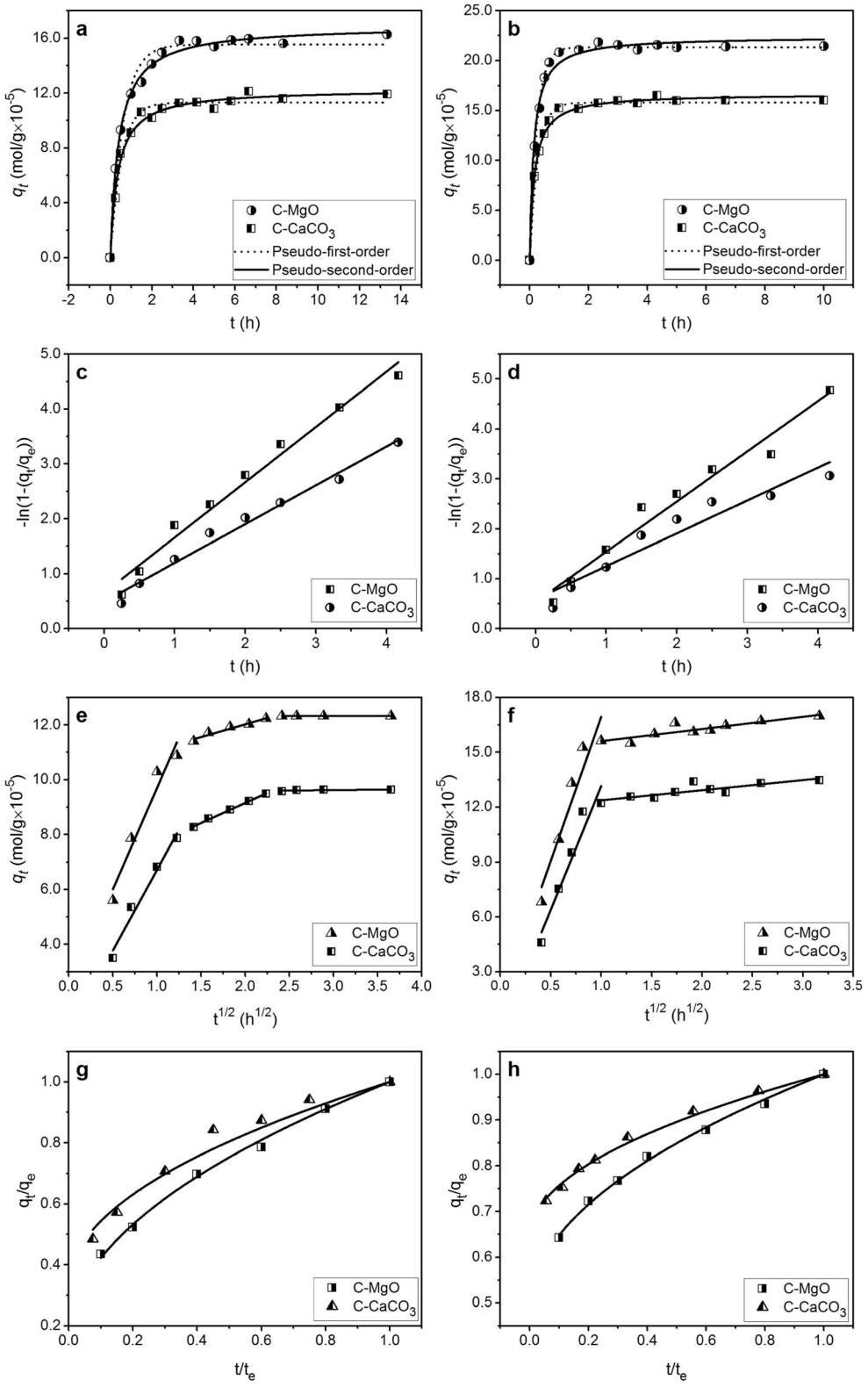

Fig. 5 Time-dependent sorption curves of **a** EBT and **b** U(VI). Liquid film diffusion model fitting of **c** EBT and **d** U(VI). Intraparticle diffusion model for **e** EBT and **f** U(VI). Initial sorption model for **g** EBT and **h** U(VI), at C_o[EBT] = 8.67×10^{-5} mol/L, C_o[U(VI)] = 7.61×10^{-5} mol/L, m/V = 0.20 g/L and T = 25°C. (pH = 2.0 for EBT sorption while pH = 6.0 and C[NaCl] = 0.01 mol/L for U(VI) sorption)

$CaCO_3$. The kinetic data agreed fairly well with the PSO simulation. The good matching of kinetic data to PSO model was further confirmed by the percent relative error factor (*RE* (%)) calculated from Eq. (3).

$$\mathrm{RE}(\%) = \frac{\left|q_{\mathrm{e,calc.}} - q_{\mathrm{e,exp.}}\right|}{q_{\mathrm{e,exp.}}} \times 100 \quad (3)$$

where $q_{\mathrm{e,calc.}}$ and $q_{\mathrm{e,exp.}}$ are the calculated and experimental adsorption capacities, respectively. The values of RE (%) for PSO were lower than that of PFO (Table S3), confirming a better fit of the PSO model to the experimental data. The agreement of kinetic data with PSO model suggested that EBT and U(VI) sorption onto C-$CaCO_3$ and C-MgO was a chemical process (Zhao et al. 2014; Zou et al. 2015) that might involve the exchange of electrons between the pollutant species and adsorbent (Khan et al. 2018). To further investigate the adsorption kinetics of EBT and U(VI) sorption, the initial adsorption rate (h (mol/g·h)) and half-equilibrium time ($t_{1/2}$ (h)) were calculated from Eqs. (4) and (5), respectively, and the results are recorded in Table S3.

$$h = k_2 q_{\mathrm{e}}^2 \quad (4)$$

$$t_{1/2} = \frac{1}{k_2 q_{\mathrm{e}}} \quad (5)$$

By changing the adsorbent from C-$CaCO_3$ to C-MgO, the h values increased from 1.61×10^{-15} to 2.01×10^{-15} mol/g·h for EBT and from 5.59×10^{-15} to 11.3×10^{-15} mol/g h for U(VI) ions, while $t_{1/2}$ values reduced from 9.0×10^{10} to 7.6×10^{10} h for EBT while this decrease for U(VI) was 3.0×10^{10} h to 2.0×10^{10} h.

Diffusion is a key phenomenon involved in the process of adsorption. The migration of the pollutant species from the bulk of the solution to the liquid film boundary of the adsorbent is referred to as the external surface adsorption. Besides this, the other processes involved in the adsorption are intraparticle diffusion and film diffusion.

The liquid diffusion model (Eq. (6)) was applied to study the film diffusion process.

$$\ln\left(1 - \frac{q_{\mathrm{t}}}{q_{\mathrm{e}}}\right) = -k_{\mathrm{fd}} t \quad (6)$$

Here, the q_t/q_e is the equilibrium sorption ratio and k_{fd} (h^{-1}) is the rate constant for sorption. The zero intercept of the straight line obtained by plotting -ln(1-q_t/q_e) vs. t represents that sorption kinetics is governed by the film diffusion process (Chen et al. 2017). However, for both EBT and U(VI) sorption these intercepts were greater than zero (Fig. 5c, d), which shows that the film diffusion was not the only process involved in the adsorption of U(VI) and EBT.

The kinetic data was also simulated by intraparticle diffusion model (IPD, Eq. (7)) (Weber and Morris 1963), to understand the role of diffusion in the adsorption process.

$$q_t = k_{\mathrm{p}i} t^{0.5} + C_{\mathrm{i}} \quad (7)$$

The values of $k_{\mathrm{p}i}$ (mol/g·$h^{1/2}$) and C_{i} (mol/g) along with R^2, obtained from Eq. (7) are tabulated in Table S3. The IPD plots obtained by using piecewise regression of q_{t} vs. $t^{0.5}$ are shown in Fig. 5e, f. They indicate that the IPD plot of EBT was comprised of three regions while that of U(VI) consisted of two regions. The values of IPD model parameters (Table S3) reveal that the adsorption rate constants were in the order of $k_{\mathrm{p1}} > k_{\mathrm{p2}} > k_{\mathrm{p3}}$. High adsorption rate in the first region was due to the availability of a large number of free adsorption sites on the adsorbent surfaces. In the second region, the rate-determining step, the adsorption rate slowed down and became almost insignificant in the third stage, where approximately all the adsorption points were covered by the pollutant species. The adsorption process is controlled by IPD when the plot of q_{t} vs. $t^{0.5}$ passes through the origin. However, Fig. 5 e and f indicate that the IPD plots did not pass through the origin, which reflected that some interactions other than IPD were also involved in EBT and U(VI) sorption (Ahmed et al. 2019). The intercept (C_{i}) is related to the boundary layer effect (McKay et al. 1980) which increases directly with the increase in C_{i}. The C_{i} values (Table S3) were in the order $C_1 < C_2 < C_3$, indicating that the boundary layer effect continued to increase from region-1 to region-3. The initial adsorption factor (R_{i}) was computed from the IPD model, which was helpful to further understand the importance of boundary layer diffusion (BLD) in the adsorption process (Wu et al. 2009). For the determination of R_{i}, Eq. (7) can be written as:

$$q_{\mathrm{e}} = k_{\mathrm{p}i} t_{\mathrm{e}}^{0.5} + C_i \quad (8)$$

where t_{e} (h) is the equilibrium time and q_{e} (mol/g) is the amount of EBT/U(VI) adsorbed at $t = t_{\mathrm{e}}$. Subtracting Eqs. (8) and (7) and on rearrangement gives Eq. (9).

$$\left(\frac{q_{\mathrm{t}}}{q_{\mathrm{e}}}\right) = 1 - R_{\mathrm{i}}\left[1 - \left(\frac{t}{t_{\mathrm{e}}}\right)^{0.5}\right] \quad (9)$$

where $R_{\mathrm{i}} = \frac{k_{\mathrm{p}i} t_{\mathrm{e}}^{0.5}}{q_{\mathrm{e}}}$ is defined as the initial adsorption factor of the IPD model. R_{i} can be obtained from Eq. (8) as:

$$R_{\mathrm{i}} = 1 - \frac{C_{\mathrm{i}}}{q_{\mathrm{e}}} \quad (10)$$

$R_{\mathrm{i}} = 1$ for $C_{\mathrm{i}} = 0$ means that there is no initial adsorption in the system and adsorption is governed merely by IPD. $R_{\mathrm{i}} = 0$ for $C_{\mathrm{i}} = q_{\mathrm{e}}$ refers to no real adsorption and some other processes such as coagulation and aggregation may involve in the system. However, as the ratio of $C_{\mathrm{i}}/q_{\mathrm{e}}$ decreases the R_{i} increases and IPD becomes the prominent adsorption mechanism. The R_{i} values, classified into four zones, are given in Table S4. In zone 0 and 1, the adsorption is controlled by IPD

Table 2 Langmuir and Freundlich model constants and correlation coefficients for the adsorption of EBT and U(VI) onto C-$CaCO_3$ and C-MgO at 25°C

Pollutant	C-$CaCO_3$				C-$CaCO_3$			
	Langmuir model				Freundlich model			
	q_m (mol/g)	b (L/mol)	R^2	RE (%)	K_F ($mol^{1-n} \cdot L^n/g$)	n	R^2	RE (%)
EBT	2.53×10^{-4}	5.70×10^4	0.995	5.06	4.26×10^{-3}	3.03	0.953	15.24
U(VI)	5.92×10^{-4}	3.10×10^4	0.982	9.65	3.20×10^{-2}	2.15	0.973	23.61
	C-MgO				C-MgO			
EBT	3.62×10^{-4}	9.65×10^4	0.988	6.51	5.31×10^{-3}	3.32	0.935	12.70
U(VI)	8.10×10^{-4}	7.14×10^4	0.985	7.58	2.67×10^{-2}	2.57	0.955	18.07

throughout the process. The adsorption reaches to about 80% in zones 2 and 3. In zone 4, the initial adsorption occupies more than 90% of the adsorption. The initial adsorption characteristic curves based on the IPD model (Eq. (9)) are presented in Fig. 5 g and h. The R_i values for EBT adsorption onto C-$CaCO_3$ and C-MgO were 0.67 and 0.84, respectively. According to Table S4, the adsorption of EBT comes into zone 2 and exhibits intermediate initial adsorption. Similarly, the R_i values for U(VI) sorption onto C-$CaCO_3$ and C-MgO were 0.35 and 0.49, respectively, which fall into zone 3 and showed strong initial adsorption. One reason for low adsorption of EBT was its larger molecular size than U(VI) (Wu et al. 2009).

Sorption isotherms and thermodynamic studies

Isotherm study of U(VI) and EBT sorption was performed at different temperatures because it affects not only the state of pollutant anions and cations but also the sorption efficiency of adsorbents. EBT and U(VI) sorption data were simulated by Langmuir (Eq. (11)) (Yang and Fox 2018) and Freundlich (Eq. (12)) (Choi et al. 2019) isotherm models.

$$q_e = \frac{q_m b C_e}{1 + b C_e} \tag{11}$$

$$q_e = K_F C_e^{\,n} \tag{12}$$

Table 3 Comparison of the adsorption capacities of different adsorbents for EBT and U(VI) calculated at 25°C

Adsorbent	pH	q_m (mol/g) EBT	References
Maize stem tissue	2.0	3.62×10^{-4}	(Vucurovic et al. 2014)
Activated carbon from waste rice hulls	2.0	3.48×10^{-4}	(de Luna et al. 2013)
MgAl-LDH	4.0	2.78×10^{-4}	(Yasin et al. 2010)
Magnetite/pectin NPs Magnetite/silica/pectin NPs	2.0	2.24×10^{-4} 1.74×10^{-4}	(Attallah et al. 2016)
$NiFe_2O_4$ nanoparticles	6.0	1.02×10^{-4}	(Moeinpour et al. 2014)
Microwave-treated almond shell Cold plasma–treated almond shell	4.0	6.37×10^{-5} 3.94×10^{-5}	(Sahin et al. 2013)
Untreated almond shell		1.31×10^{-5}	
C-$CaCO_3$ C-MgO	2.0	2.53×10^{-4} 3.62×10^{-4}	This work
		q_m (mol/g) U(VI)	
SBA/SA SBA/EnSA	4.0	1.37×10^{-4} 2.67×10^{-4}	(Dolatyari et al. 2016)
Fe_3O_4/BMSPN composite	6.0	2.51×10^{-4}	(Zhang et al. 2012)
GO GO/MnO_2	3.8 3.8	6.12×10^{-4} 6.75×10^{-4}	(Pan et al. 2016)
Carbonaceous nanofibers	4.5	7.66×10^{-4}	(Sun et al. 2016)
Fe_3O_4/amino-GO	5.9	7.90×10^{-4}	(Chen et al. 2016)
GO-S	3.0	1.06×10^{-3}	(Pan et al. 2017)
C-$CaCO_3$ C-MgO	6.0	5.92×10^{-4} 8.10×10^{-4}	This work

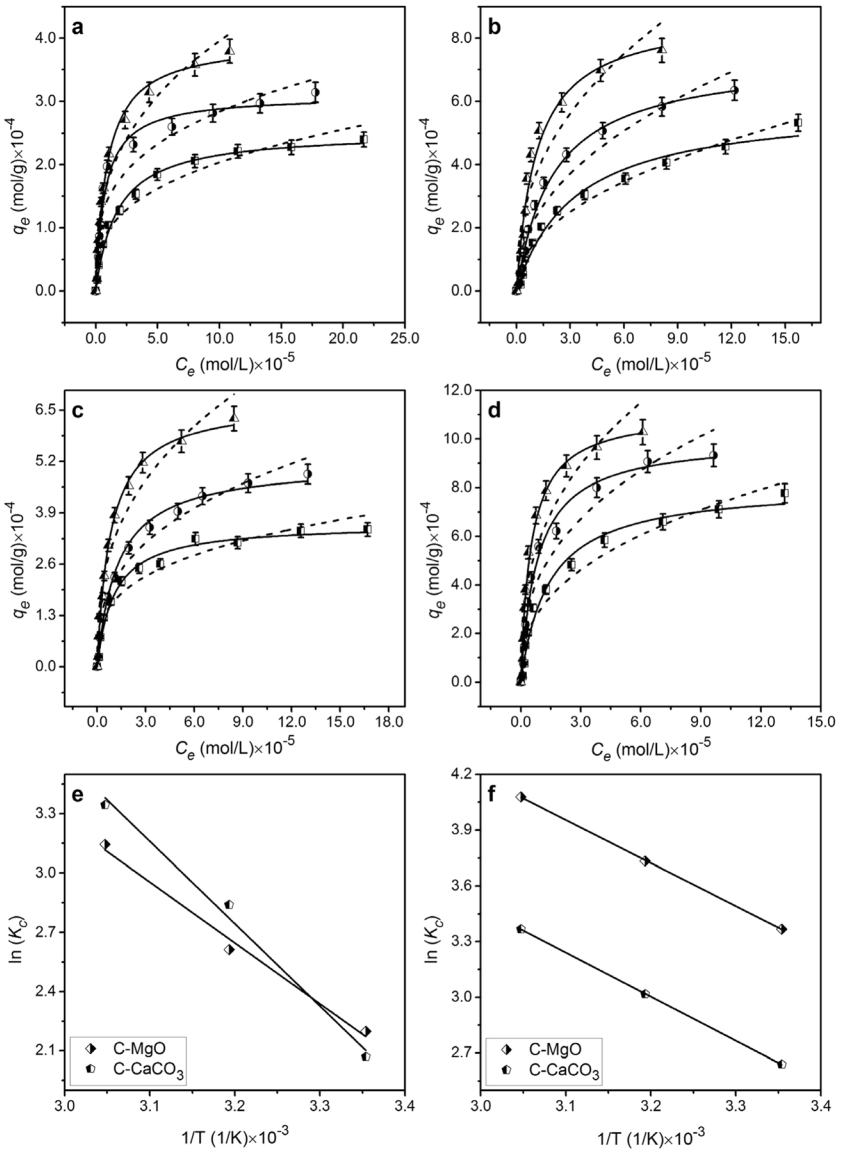

Fig. 6 Sorption curves of **a** EBT and **b** U(VI) onto C-$CaCO_3$, sorption curves of **c** EBT and **d** U(VI) onto C-MgO at m/V = 0.20 g/L and contact time = 24 h, pH = 2.0 for EBT sorption while pH = 6.0 and C[NaCl] = 0.01 mol/L for U(VI) sorption, ■=25°*C*, ◑=40°C, and ◭=55°C, solid line: Langmuir model, dash line: Freundlich model. van't Hoff plots for **e** EBT and **f** U(VI) sorption

where q_m (mol/g) is the monolayer maximum adsorption, C_e (mol/L) is the equilibrium concentration of pollutants in solution, b (L/mol), K_F (mol^{1-n}·L^n/g) and n are the constants of relative models.

Langmuir isotherm is useful to describe homogeneous adsorption. It was applied to calculate the monolayer maximum adsorption capacity of C-$CaCO_3$ and C-MgO for EBT and U(VI) ions. Freundlich isotherm was applied to depict the heterogeneity of EBT and U(VI) sorption onto C-$CaCO_3$ and C-MgO surfaces. Table 2 encloses the values of the respective parameters of the Langmuir and Freundlich models calculated at 25°C, while those calculated at 40 and 55°C are listed in Table S5. The values of n indicated that EBT and U(VI) sorption onto C-$CaCO_3$ and C-MgO was a favourable process (Dada et al. 2012). However, the data did not converge well with the Freundlich model and the regression coefficient was lower as compared to the Langmuir isotherm model. The better fit of the Langmuir model was further confirmed by the relative error factor, calculated from Eq. (3). As shown in Table 2, the RE (%) values for Langmuir model were lower than those of the Freundlich model, indicating a better fit of the sorption data to the Langmuir model. Moreover, it was proved with an important characteristic of the Langmuir model namely the dimensionless constant separation factor (R_L), that the adsorption of EBT and U(VI) onto C-$CaCO_3$ and C-MgO was a favourable process (detail is given in SI).

The monolayer adsorption capacities of C-$CaCO_3$ and C-MgO calculated at 25°C were 2.53×10^{-4} and $3.62 \times$

10^{-4} mol/g for EBT and 5.92×10^{-4} and 8.10×10^{-4} mol/g for U(VI) ions, respectively. Table 3 shows that C-$CaCO_3$ and C-MgO has comparatively good adsorption abilities for EBT and U(VI) ions. The EBT and U(VI) sorption isotherms at 25, 40 and 55°C are presented in Fig. 6a–d. The rapid increase in the adsorption capacity with increasing temperature suggested that EBT and U(VI) sorption was more favourable at high temperature.

Thermodynamic study was helpful in explaining the feasibility of sorption reaction. The Van't Hoff Eq. (13) was applied to calculate the important thermodynamic parameters, the standard entropy change (ΔS°, J/mol·K) and standard enthalpy change (ΔH°, kJ/mol).

$$\ln\frac{C_a}{C_e} = lnK_c = \frac{\Delta S^{\circ}}{R} - \frac{\Delta H^{\circ}}{R} \times \frac{1}{T} \quad (13)$$

where C_a (mol/L), K_c, T (K) and R (8.314 J/mol·K) are the solid phase equilibrium concentration, equilibrium constant, thermodynamic temperature and universal gas constant, respectively. The plots of lnK_c vs. $1/T$ (Fig. 6e, f) gave a straight line with intercept and slope equal to $\Delta S^{\circ}/R$ and $\Delta H^{\circ}/R$, respectively. The change in standard Gibbs free energy of adsorption (ΔG°, kJ/mol) was measured from Eq. (14):

$$\Delta G^{\circ} = \Delta H^{\circ} - T\Delta S^{\circ} \quad (14)$$

Table 4 shows the values of thermodynamic parameters obtained from Eqs. (13) and (14). The negative values of ΔG° and positive values of ΔH° and ΔS° revealed that sorption of EBT and U(VI) onto C-$CaCO_3$ and C-MgO was spontaneous, endothermic and random at solid-solution interface. The decrease in ΔG° values with increasing temperature proved that sorption became more favourable at high temperature due to the dehydration of the pollutant ions (Liu et al. 2015). The results obtained at 25, 40 and 55°C displayed that the adsorption of EBT and U(VI) on both adsorbents increased with the increase in temperature, which might be attributed to the tendency of the pollutant species to escape from the bulk phase to the solid phase.

DFT calculations

The DFT theoretical calculations (Gonze et al. 2009) were important to explore the interaction mechanism of EBT and U(VI) ions with MgO and $CaCO_3$ at the molecular level. The geometric optimization, sorption energy calculation and charge density analysis were performed by Vienna ab initio Simulation Package (VASP) (Kresse and Furthmüller 1996). The exchange-correction function was described by the Perdew-Burke-Ernzerhof (PBE) formulation of the generalized gradient approximation (GGA) (Perdew et al. 1996). Crystal structures and other DFT conditions are given in the SI.

Figure 7 represents the most stable geometries for EBT and U(VI) sorption onto MgO and $CaCO_3$. As shown in Fig. 7 a and b, EBT molecule orients parallel to the adsorbent's surface. The distance between EBT and $CaCO_3$ (1.778 Å) was much shorter than that of EBT and MgO (4.354 Å). However, Mg-O(EBT) bond length (2.178 Å) was shorter than Ca-O(EBT) bonds, i.e., Ca1-O1 (2.713 Å), Ca1-O2 (2.457 Å), Ca2-O3 (2.474 Å) and Ca2-O4 (3.522 Å). Similarly, the U1-O1 distance in MgO system (2.099 Å) was shorter than that of $CaCO_3$ system (2.271 Å, Fig. 7c, d). Therefore, from a geometric perspective, the electrostatic interactions of EBT and U(VI) with MgO were much stronger than $CaCO_3$. The sorption energy (ΔE) was calculated from $\Delta E = E_{sub} + E_{EBT/U} - E_{comp}$, where E_{comp} represents the total energy of the target complex system, E_{sub} and $E_{EBT/U}$ correspond to the energies of the substrate ($CaCO_3$ or MgO) and the isolated EBT or U(VI) molecules, respectively. High sorption energy of EBT-MgO (20.62 kcal/mol) than EBT-$CaCO_3$ (10.21 kcal/mol), and that of U-MgO

Table 4 Thermodynamic parameters for EBT and U(VI) sorption on C-$CaCO_3$ and C-MgO

	T (K)	K_c	ΔG° (kJ/mol)	ΔH° (kJ/mol)	ΔS° (J/mol·K)
EBT at C-$CaCO_3$	298.15	7.92	− 5.21	34.69	0.134
	313.15	17.11	− 7.22		
	328.15	28.37	− 9.23		
EBT at C-MgO	298.15	9.00	− 5.38	25.63	0.104
	313.15	13.63	− 6.94		
	328.15	23.22	− 8.50		
U(VI) at C-$CaCO_3$	298.15	14.00	− 6.54	19.74	0.088
	313.15	20.43	− 7.86		
	328.15	29.00	− 9.18		
U(VI) at C-MgO	298.15	29.00	− 8.34	19.25	0.093
	313.15	41.86	− 9.73		
	328.15	59.00	− 11.12		

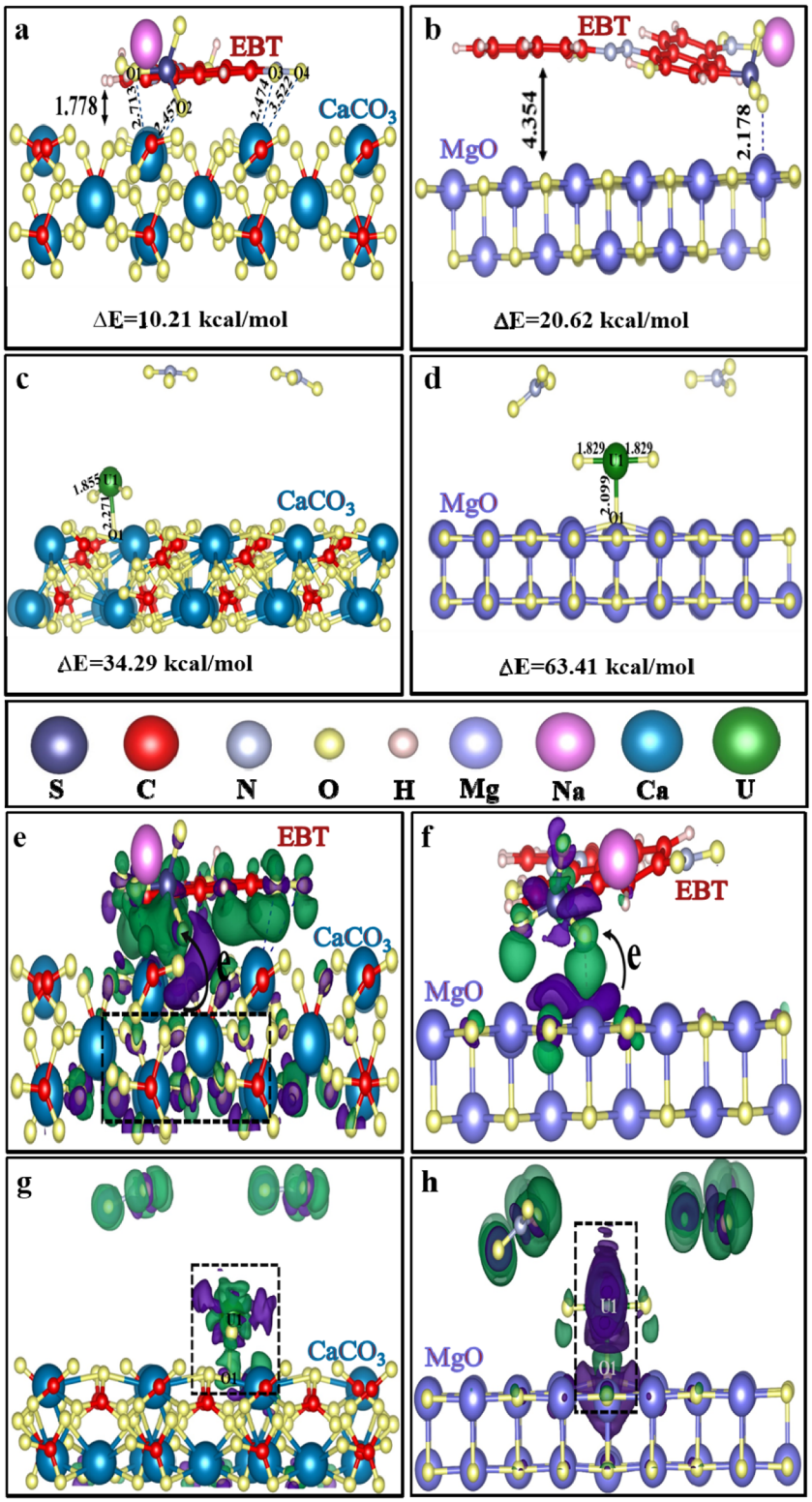

Fig. 7 Geometric structures of the complexes of **a** EBT-$CaCO_3$, **b** EBT-MgO, **c** U-$CaCO_3$ and **d** U-MgO. The charge density differences of **e** EBT-$CaCO_3$ system, **f** EBT-MgO system, **g** U-$CaCO_3$ system and **h** U-MgO system. Purple and green colours represent positive and negative charges, respectively, and all bond lengths and distances are given in Å

(63.41 kcal/mol) than U-$CaCO_3$ (34.29 kcal/mol) indicated that the sorption ability of MgO for EBT and U(VI) was better than that of $CaCO_3$.

In order to further clarify the adsorption mechanism, the differential charge density distributions of both adsorption systems were calculated as depicted in Fig. 7e–h. The

three-dimensional charge density difference plot with an isosurface value of 1.0×10^{-5} e·Å^3 was obtained by subtracting the calculated electronic charge of the individual parts. The green isosurface represented the regions where the electron density was increased while the purple one represented a reduction in the charge density. In case of EBT, the adsorption process induced the intra- and intermolecular charge redistribution not only in the EBT molecules but also in the basal plane of $CaCO_3$. While in the case of U(VI), the uranyl ions (UO_2^{2+}) were positively charged and the charge transfer process took place only in the type of "atom to atom". The results of charge density distribution showed that the electrostatic interactions in EBT-MgO and U-MgO were stronger than EBT-$CaCO_3$ and U-$CaCO_3$, which were consistent with the experimental results. Short bond distances, high sorption energies and increased charge density all support high sorption ability of MgO for both EBT and U(VI) as compared to $CaCO_3$.

Reusability

Reusability is an important property of an adsorbent which reduces the cost of the adsorption process. Both C-$CaCO_3$ and C-MgO were recycled five times to check their reusability for EBT and U(VI) sorption. After the adsorption of EBT, 1.0 g of C-$CaCO_3$ and C-MgO was stirred in 15 mL NaOH (1.0 mol/L) and shaken at 25°C. After 24 h, the adsorbents were separated from the solution and washed with 15 mL Milli-Q water followed by 10 mL ethanol and finally dried at 110°C for 5 h. The dried mass was reused for the adsorption of EBT and the results are presented in Fig. 8. It indicates that in five cycles, the adsorption capacity of C-$CaCO_3$ and C-MgO for EBT decreased by 15.4 and 11.2%

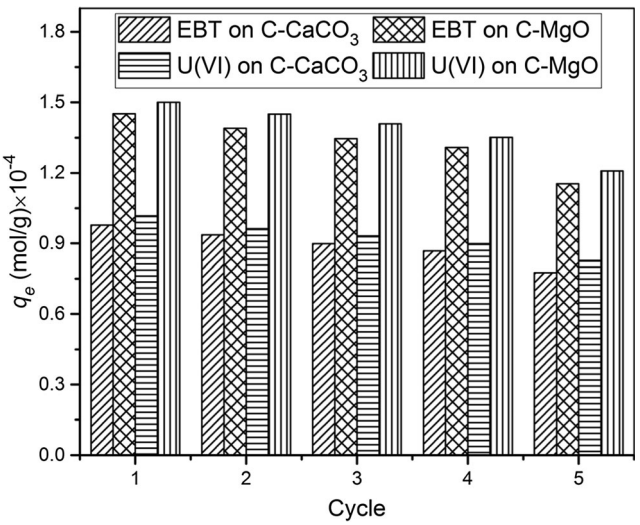

Fig. 8 Recyclability of C-$CaCO_3$ and C-MgO for the removal of EBT and U(VI) ions from water solutions at C_o[EBT] = 8.67×10^{-5} mol/L, C_o[U(VI)] = 7.61×10^{-5} mol/L, m/V = 0.20 g/L, contact time = 24 h and T = 25°C. (pH = 2.0 for EBT sorption, while pH = 6.0 and C[NaCl] = 0.01 mol/L for U(VI) sorption)

respectively. The big decrease in adsorption capacity of C-$CaCO_3$ was due to its strong complexation with EBT. Like EBT, the same process was repeated for the desorption of U(VI), however, instead of NaOH, 1.0 mol/L HCl was used as eluent. Figure 8 shows that in the first three cycles, the sorption capacities of C-$CaCO_3$ and C-MgO for U(VI) decreased by 8.5 and 6.1% respectively, while in the fourth and fifth cycle, these decreased by 13.7 and 10.3% respectively. The reason for the big decrease in the adsorption ability in the fourth and fifth cycle would be due to the corrosion of the adsorbents in acidic medium and incomplete separation of the pollutant species. These results indicate that both adsorbents can be reused five times for the effective elimination of EBT and U(VI) from wastewater.

Conclusion

In this study, EBT and U(VI) sorption onto C-$CaCO_3$ and C-MgO was explored by batch technique and DFT theoretical calculations. The adsorption of EBT and U(VI) ions was pH dependent; however, ionic strength had little effect (0.6%) on the adsorption process. The adsorption amount of EBT and U(VI) both raised with the increasing amount of adsorbents and reached its maximum value at 0.20 g/L of adsorbent. This showed that satisfying adsorption results could be achieved with small amounts of C-$CaCO_3$ and C-MgO. The adsorption data of EBT and U(VI) well agreed with PSO kinetic and Langmuir isotherm models. Thermodynamically, the adsorption reaction of EBT and U(VI) on the surfaces of C-$CaCO_3$ and C-MgO was favourable. Results of the sorption data of both EBT and U(VI) were concordant with DFT calculations. It can be concluded from the easy preparation, strong interactions with EBT and U(VI) and reusability that both C-$CaCO_3$ and C-MgO can be useful adsorbents in the possible environmental pollution cleanup.

Funding information This study was financially supported by the China Postdoctoral Science Foundation (2018M641293) for foreign PhD scholars, the NCEPU "Double First-Class" Talent Cultivation Program (XM1805405) and the National Key Research and Development Program of China (2017YFA0207002).

References

Ahmed MJ, Okoye PU, Hummadi EH, Hameed BH (2019) High-performance porous biochar from the pyrolysis of natural and renewable seaweed (*Gelidiella acerosa*) and its application for the adsorption of methylene blue. Bioresour Technol 278:159–164. https://doi.org/10.1016/j.biortech.2019.01.054

Attallah O, Al-Ghobashy M, Nebsen M, Salem M (2016) Removal of cationic and anionic dyes from aqueous solution with magnetite/pectin and magnetite/silica/pectin hybrid nanocomposites: kinetic, isotherm and mechanism analysis. RSC Advances 6:11461–11480. https://doi.org/10.1039/c5ra23452b

Ayub K et al (2017) The role of graphene oxide and graphene oxide-based nanomaterials in the removal of pharmaceuticals from aqueous media: a review. Environ Sci Pollut R 24:7938–7958. https://doi.org/10.1007/s11356-017-8388-8

Balasubramanian UM, Vaiyazhipalayam Murugaiyan S, Marimuthu T (2019) Enhanced adsorption of Cr(VI), Ni(II) ions from aqueous solution using modified Eichhornia crassipes and *Lemna minor*. Environ Sci Pollut Res Int. https://doi.org/10.1007/s11356-019-06357-7

Bayramoglu G, Akbulut A, Arica MY (2015) Study of polyethyleneimine- and amidoxime-functionalized hybrid biomass of Spirulina (Arthrospira) platensis for adsorption of uranium (VI) ion. Environ Sci Pollut Res Int 22:17998–18010. https://doi.org/10.1007/s11356-015-4990-9

Blaisi NI et al (2018) Date palm ash-MgAl-layered double hydroxide composite: sustainable adsorbent for effective removal of methyl orange and eriochrome black-T from aqueous phase. Environ Sci Pollut Res Int 25:34319–34331. https://doi.org/10.1007/s11356-018-3367-2

Chen J, Xiang L (2009) Controllable synthesis of calcium carbonate polymorphs at different temperatures. Powder Technol 189:64–69. https://doi.org/10.1016/j.powtec.2008.06.004

Chen L, Zhao D, Chen S, Wang X, Chen C (2016) One-step fabrication of amino functionalized magnetic graphene oxide composite for uranium(VI) removal. J Colloid Interf Sci 472:99–107. https://doi.org/10.1016/j.jcis.2016.03.044

Chen Z et al (2017) Synthesis of magnetic Fe_3O_4/CFA composites for the efficient removal of U(VI) from wastewater. Chem Eng J 320:448–457. https://doi.org/10.1016/j.cej.2017.03.074

Chen Y et al (2018) The properties of fibreboard based on nanolignocelluloses/$CaCO_3$/PMMA composite synthesized through mechano-chemical method. Sci Rep 8:5121. https://doi.org/10.1038/s41598-018-23497-x

Child DP, Hotchkis MAC (2013) Plutonium and uranium contamination in soils from former nuclear weapon test sites in Australia. NUCL Instum Meth B 294:642–646. https://doi.org/10.1016/j.nimb.2012.05.018

Choi YL, Choi JS, Lingamdinne LP, Chang YY, Koduru JR, Ha JH, Yang JK (2019) Removal of U(VI) by sugar-based magnetic pseudo-graphene oxide and its application to authentic groundwater using electromagnetic system. Environ Sci Pollut Res Int 26:22323–22337. https://doi.org/10.1007/s11356-019-05260-5

Chu DH et al (2013) CO_2 mineralization into different polymorphs of $CaCO_3$ using an aqueous-CO_2 system. RSC Advances 3:21722. https://doi.org/10.1039/c3ra44007a

Cui W, Li P, Wang Z, Zheng S, Zhang Y (2018) Adsorption study of selenium ions from aqueous solutions using MgO nanosheets synthesized by ultrasonic method. J Hazard Mater 341:268–276. https://doi.org/10.1016/j.jhazmat.2017.07.073

Dada AO, Olalekan AP, Olatunya AM, DADA O (2012) Langmuir, Freundlich, Temkin and Dubinin-Radushkevich isotherms studies of equilibrium sorption of Zn^{2+} unto phosphoric acid modified rice husk. IOSR-JAC 3:38–45. https://doi.org/10.9790/5736-0313845

de Luna MDG, Flores ED, Genuino DAD, Futalan CM, Wan MW (2013) Adsorption of eriochrome black T (EBT) dye using activated carbon prepared from waste rice hulls-optimization, isotherm and kinetic studies. J Taiwan Inst Chem E 44:646–653. https://doi.org/10.1016/j.jtice.2013.01.010

Devi RR, Umlong IM, Raul PK, Das B, Banerjee S, Singh L (2012) Defluoridation of water using nano-magnesium oxide. J Exp Nanosci 9:512–524. https://doi.org/10.1080/17458080.2012.675522

Ding C, Cheng W, Sun Y, Wang X (2015) Effects of Bacillus subtilis on the reduction of U(VI) by nano-Fe^0. Geochim Cosmochim Acta 165:86–107. https://doi.org/10.1016/j.gca.2015.05.036

Dolatyari L, Yaftian MR, Rostamnia S (2016) Removal of uranium(VI) ions from aqueous solutions using Schiff base functionalized SBA-15 mesoporous silica materials. J Environ Manag 169:8–17. https://doi.org/10.1016/j.jenvman.2015.12.005

Dushenkov S, Vasudev D, Kapulnik Y, Gleba D, Fleisher D, Ting KC, Ensley B (1997) Removal of uranium from water using terrestrial plants. Environ Sci Technol 31:3468–3474. https://doi.org/10.1021/es970220l

Forgacs E, Cserhati T, Oros G (2004) Removal of synthetic dyes from wastewaters: a review. Environ Int 30:953–971. https://doi.org/10.1016/j.envint.2004.02.001

Gonze X et al (2009) ABINIT: First-principles approach to material and nanosystem properties. Comput Phys Commun 180:2582–2615. https://doi.org/10.1016/j.cpc.2009.07.007

Goryczka T, Dercz G, Prusik K, Pajak L, Lagiewka E (2010) Crystallite size determination of MgO nanopowder from X-Ray diffraction patterns registered in GIXD technique. Solid State Phenom 163:177–182. https://doi.org/10.4028/www.scientific.net/SSP.163.177

Hao X, Quach L, Korah J, Spieker WA, Regalbuto JR (2004) The control of platinum impregnation by PZC alteration of oxides and carbon. J Mol Catal A Chem 219:97–107. https://doi.org/10.1016/j.molcata.2004.04.026

Houas A, Lachheb H, Ksibi M, Elaloui E, Guillard C, Herrmann J-M (2001) Photocatalytic degradation pathway of methylene blue in water. Appl Catal B Environ 31:145–157. https://doi.org/10.1016/S0926-3373(00)00276-9

Hu J, Song Z, Chen L, Yang H, Li J, Richards R (2010) Adsorption properties of MgO(111) nanoplates for the dye pollutants from wastewater. J Chem Eng Data 55:3742–3748. https://doi.org/10.1021/je100274e

Hu R, Wang X, Dai S, Shao D, Hayat T, Alsaedi A (2015) Application of graphitic carbon nitride for the removal of Pb(II) and aniline from aqueous solutions. Chem Eng J 260:469–477. https://doi.org/10.1016/j.cej.2014.09.013

Khan A et al (2018) Novel magnetite nanorod-decorated Si-Schiff base complex for efficient immobilization of U(VI) and Pb(II) from water solutions. Dalton Trans 47:11327–11336. https://doi.org/10.1039/C8DT01213J

Khurana I, Shaw AK, Bharti KJM, Rai PK (2018) Batch and dynamic adsorption of Eriochrome black T from water on magnetic graphene oxide: experimental and theoretical studies. J Environ Chem Eng 6:468–477. https://doi.org/10.1016/j.jece.2017.12.029

Kodama S, Sekiguchi H (2006) Estimation of point of zero charge for activated carbon treated with atmospheric pressure non-thermal oxygen plasmas. Thin Solid Films 506-507:327–330. https://doi.org/10.1016/j.tsf.2005.08.137

Konietzka R (2015) Gastrointestinal absorption of uranium compounds-a review. Regul Toxicol Pharm 71:125–133. https://doi.org/10.1016/j.yrtph.2014.08.012

Kresse G, Furthmüller J (1996) Efficient iterative schemes for ab initio total-energy calculations using a plane-wave basis set. Phys Rev B 54:11169–11186. https://doi.org/10.1103/PhysRevB.54.11169

Li LX, Xu D, Li XQ, Liu WC, Jia Y (2014) Excellent fluoride removal properties of porous hollow MgO microspheres. New J Chem 38:5445–5452. https://doi.org/10.1039/C4NJ01361A

Liao W et al (2019) MnO_2-loaded microorganism-derived carbon for U(VI) adsorption from aqueous solution. Environ Sci Pollut Res Int 26:3697–3705. https://doi.org/10.1007/s11356-018-3887-9

Liu X, Li J, Wang X, Chen C, Wang X (2015) High performance of phosphate-functionalized graphene oxide for the selective adsorption of U(VI) from acidic solution. J Nucl Mater 466:56–64. https://doi.org/10.1016/j.jnucmat.2015.07.027

Loera-Serna S, Ortiz E, Beltran HI (2017) First trial and physicochemical studies on the loading of basic fuchsin, crystal violet and Black

Eriochrome T on HKUST-1. New J Chem 41:3097–3105. https://doi.org/10.1039/C6NJ03912J

Mageshwari K, Mali SS, Sathyamoorthy R, Patil PS (2013) Template-free synthesis of MgO nanoparticles for effective photocatalytic applications. Powder Technol 249:456–462. https://doi.org/10.1016/j.powtec.2013.09.016

McKay G, Otterburn MS, Sweeney AG (1980) The removal of colour from effluent using various adsorbents-III. Silica: Rate processes. Water Res 14:15–20. https://doi.org/10.1016/0043-1354(80)90037-8

Moeinpour F, Alimoradi A, Kazemi M (2014) Efficient removal of Eriochrome black-T from aqueous solution using $NiFe_2O_4$ magnetic nanoparticles. J Environ Health Sci 12:1–7. https://doi.org/10.1186/s40201-014-0112-8

Moussavi G, Mahmoudi M (2009) Removal of azo and anthraquinone reactive dyes from industrial wastewaters using MgO nanoparticles. J Hazard Mater 168:806–812. https://doi.org/10.1016/j.jhazmat.2009.02.097

Nassar MY, Mohamed TY, Ahmed IS, Samir I (2017) MgO nanostructure via a sol-gel combustion synthesis method using different fuels: an efficient nano-adsorbent for the removal of some anionic textile dyes. J Mol Liq 225:730–740. https://doi.org/10.1016/j.molliq.2016.10.135

Ni M, Ratner BD (2008) Differentiating calcium carbonate polymorphs by surface analysis techniques-an XPS and TOF-SIMS study. Surf Interface Anal 40:1356–1361. https://doi.org/10.1002/sia.2904

Ohmichi T, Fukushima S, Maeda A, Watanabe H (1981) On the relation between lattice parameter and O/M ratio for uranium dioxide-trivalent rare earth oxide solid solution. J Nucl Mater 102:40–46. https://doi.org/10.1016/0022-3115(81)90544-4

Oliveira LCA, Rios RVRA, Fabris JD, Garg V, Sapag K, Lago RM (2002) Activated carbon/iron oxide magnetic composites for the adsorption of contaminants in water. Carbon 40:2177–2183. https://doi.org/10.1016/S0008-6223(02)00076-3

Pan N et al (2016) Preparation of graphene oxide-manganese dioxide for highly efficient adsorption and separation of Th(IV)/U(VI). J Hazard Mater 309:107–115. https://doi.org/10.1016/j.jhazmat.2016.02.012

Pan N, Li L, Ding J, Wang R, Jin Y, Xia C (2017) A Schiff base/quaternary ammonium salt bifunctional graphene oxide as an efficient adsorbent for removal of Th (IV)/U (VI). J Colloid Interf Sci 508:303–312. https://doi.org/10.1016/j.jcis.2017.08.068

Peng H et al (2013) Preparation of hierarchical mesoporous $CaCO_3$ by a facile binary solvent approach as anticancer drug carrier for etoposide. Nanoscale Res Lett 8:321. https://doi.org/10.1186/1556-276X-8-321

Perdew JP, Burke K, Ernzerhof M (1996) Generalized gradient approximation made simple. Phys Rev Lett 77:3865–3868. https://doi.org/10.1103/PhysRevLett.77.3865

Rajan AS, Sampath S, Shukla AK (2014) An in situ carbon-grafted alkaline iron electrode for iron-based accumulators. Energy Environ Sci 7:1110–1116. https://doi.org/10.1039/c3ee42783h

Robinson T, McMullan G, Marchant R, Nigam P (2001) Remediation of dyes in textile effluent: a critical review on current treatment technologies with a proposed alternative. Bioresour Technol 77:247–255. https://doi.org/10.1016/S0960-8524(00)00080-8

Sahin O, Saka C, Kutluay S (2013) Cold plasma and microwave radiation applications on almond shell surface and its effects on the adsorption of Eriochrome Black T J. Ind Eng Chem 19:1617–1623. https://doi.org/10.1016/j.jiec.2013.01.032

Saraya MESI, Rokbaa HHAL (2016) Preparation of vaterite calcium carbonate in the form of spherical nano-size particles with the aid of polycarboxylate superplasticizer as a capping agent. Am J Nanomater 4:44–51. https://doi.org/10.12691/ajn-4-2-3

Seo KS, Han C, Wee JH, Park JK, Ahn JW (2005) Synthesis of calcium carbonate in a pure ethanol and aqueous ethanol solution as the solvent. J Cryst Growth 276:680–687. https://doi.org/10.1016/j.jcrysgro.2004.11.416

Smiciklas I, Dimovic S, Sljivic M, Plecas I (2008) The batch study of Sr^{2+} sorption by bone char. J Environ Sci Health A Toxic Hazard Subst Environ Eng 43:210–217. https://doi.org/10.1080/10934520701781624

Sun YB, Wu ZY, Wang XX, Ding CC, Cheng WC, Yu SH, Wang XK (2016) Macroscopic and microscopic investigation of U(VI) and Eu(III) adsorption on carbonaceous nanofibers. Environ Sci Technol 50:4459–4467. https://doi.org/10.1021/acs.est.6b00058

Vilela PB, Dalalibera A, Duminelli EC, Becegato VA, Paulino AT (2018) Adsorption and removal of chromium (VI) contained in aqueous solutions using a chitosan-based hydrogel. Environ Sci Pollut Res Int. https://doi.org/10.1007/s11356-018-3208-3

Vucurovic VM, Razmovski RN, Miljic UD, Puskas VS (2014) Removal of cationic and anionic azo dyes from aqueous solutions by adsorption on maize stem tissue. J Taiwan Inst Chem E 45:1700–1708. https://doi.org/10.1016/j.jtice.2013.12.020

Wang X et al (2016) High sorption of U(VI) on graphene oxides studied by batch experimental and theoretical calculations. Chem Eng J 287:448–455. https://doi.org/10.1016/j.cej.2015.11.066

Wang J et al (2017) Preparation of molybdenum disulfide coated Mg/Al layered double hydroxide composites for efficient removal of chromium(VI). ACS Sustain Chem Eng 5:7165–7174. https://doi.org/10.1021/acssuschemeng.7b01347

Weber WJ, Morris JC (1963) Kinetics of adsorption on carbon from solution. J Sanit Eng Div 89:31–60

Wu FC, Tseng RL, Juang RS (2009) Initial behavior of intraparticle diffusion model used in the description of adsorption kinetics. Chem Eng J 153:1–8. https://doi.org/10.1016/j.cej.2009.04.042

Yang K, Fox J (2018) DPF soot as an adsorbent for Cu(II), Cd(II), and Cr(VI) compared with commercial activated carbon. Environ Sci Pollut Res Int 25:8620–8635. https://doi.org/10.1007/s11356-017-1122-8

Yao HB, Li Y, Wee ATS (2000) An XPS investigation of the oxidation/corrosion of melt-spun Mg. Appl Surf Sci 158:112–119. https://doi.org/10.1016/S0169-4332(99)00593-0

Yasin Y, Abdul Malek AH, Sumari SM (2010) Adsorption of eriochrome black dye from aqueous solution onto anionic layered double hydroxides. Orient J Chem 26:1293–1298

Yin L et al (2017) Synthesis of layered titanate nanowires at low temperature and their application in efficient removal of U(VI). Environ Pollut 226:125–134. https://doi.org/10.1016/j.envpol.2017.03.078

Zhang X, Jiao C, Wang J, Liu Q, Li R, Yang P, Zhang M (2012) Removal of uranium(VI) from aqueous solutions by magnetic Schiff base: Kinetic and thermodynamic investigation. Chem Eng J 198–199:412–419. https://doi.org/10.1016/j.cej.2012.05.090

Zhao Y, Li J, Zhao L, Zhang S, Huang Y, Wu X, Wang X (2014) Synthesis of amidoxime-functionalized Fe_3O_4@SiO_2 core-shell magnetic microspheres for highly efficient sorption of U(VI). Chem Eng J 235:275–283. https://doi.org/10.1016/j.cej.2013.09.034

Zou YD, Cao XH, Luo XP, Liu Y, Hua R, Liu YH, Zhang ZB (2015) Recycle of U(VI) from aqueous solution by situ phosphorylation mesoporous carbon. J Radioanal Nucl Chem 306:515–525. https://doi.org/10.1007/s10967-015-4133-2

Zou Y et al (2017) Glycerol-modified binary layered double hydroxide nanocomposites for uranium immobilization via extended X-ray absorption fine structure technique and density functional theory calculation. ACS Sustain Chem Eng 5:3583–3595. https://doi.org/10.1021/acssuschemeng.7b00439

Publisher's note Springer Nature remains neutral with regard to jurisdictional claims in published maps and institutional affiliations.